Redshift gaps in one-dimensional photonic crystals containing hyperbolic metamaterials

Feng Wu,[1] Guang Lu,[2] Zhiwei Guo,[1] Haitao Jiang,[1,*] Chunhua Xue,[3] Minjia Zheng,[2] Chaoxin Chen,[2] Guiqiang Du,[2,4,†] and Hong Chen[1]

[1]*MOE Key Laboratory of Advanced Micro-Structured Materials, School of Physics Science and Engineering, Tongji University, Shanghai 200092, China*

[2]*School of Space Science and Physics, Shandong University at Weihai, Weihai 264209, China*

[3]*School of Computer Science & Communication Engineering, Guangxi University of Science and Technology, Liuzhou, Guangxi 545006, China*

[4]*State Key Laboratory of Surface Physics and Department of Physics, Key Laboratory of Micro and Nano-Photonic Structures (Ministry of Education), Fudan University, Shanghai 200433, China*

(Received 1 August 2018; revised manuscript received 29 September 2018; published 10 December 2018)

In conventional all-dielectric one-dimensional photonic crystals (1DPCs), photonic gaps will shift toward short wavelengths (blueshift) as the incident angle increases for both transverse magnetic (TM) and transverse electric (TE) polarizations. We theoretically and experimentally achieve redshift gaps in 1DPCs composed of alternative hyperbolic metamaterials (HMMs) and dielectrics for TM polarization based on the anomalous wavevector dispersion of HMMs. The HMM is mimicked by layered titanium dioxide and silver with a subwavelength unit cell. However, the gaps remain to be blue-shifted for TE polarization. Therefore, the edges of such gaps can be utilized for high-efficiency wide-angle polarization selection. We achieve efficient polarization selection for incident angles ranging from 50° to 80° at the wavelength of 365 nm.

DOI: 10.1103/PhysRevApplied.10.064022

I. INTRODUCTION

Photonic crystals (PCs), artificial structures with periodic modulation in the refractive index, have attracted tremendous attention because of their tremendous numbers of applications in spontaneous emission control [1,2], localization of photons [3,4], and optical circuit devices [5–10]. They can create ranges of frequencies known as photonic band gaps (PBGs) where light is totally reflected by the PCs. The conventional one-dimensional photonic crystals (1DPCs) are the simplest PCs that are composed of two kinds of dielectrics. In 1DPCs, the propagating phase within a unit cell depends on the incident angle. For a fixed wavelength, both of the phases in the propagating direction in two kinds of dielectrics will decrease as the incident angle increases, owing to the fact that the iso-frequency curve of the isotropic dielectric is circular. Therefore, the PBGs will shift toward short wavelengths to maintain the Bragg condition [11]. We call such conventional PBGs blueshift gaps. Can we overcome this physical limitation to realize redshift gaps?

Recent emergent metamaterials with tailored photonic dispersions provide this possibility. In particular, one class of metamaterials with hyperbolic dispersion called hyperbolic metamaterials (HMMs) possesses the ability to manipulate the propagation properties of electromagnetic waves. They can enhance the spontaneous decay rate of light [12–14] and realize super-resolution imaging [15–17] and unconventional microcavities [18–21]. Very recently, Xue *et al.* found that the anomalous wavevector dispersion of HMMs can be used to tune the propagating phases in 1DPCs containing HMMs and realize angle-independent gaps (i.e., zeroshift gaps) [22,23]. In HMM mimicked by a subwavelength metal-dielectric multilayer, the iso-frequency curve is a hyperbola for transverse magnetic (TM) polarization [24,25]. Therefore, the propagating phase in HMM will increase when the incident angle increases. If the phase variation in HMM can compensate that in dielectric, the gap will be invariant with the incident angles. In fact, in addition to providing a phase variation compensation effect to realize zeroshift gaps, HMMs have more freedom to tune the angle-dependent properties of the gaps.

In this paper, we explore the possibilities of realizing another kind of gap called redshift gaps in 1DPCs containing layered HMMs mimicked by subwavelength metal-dielectric stacks. This kind of gap will shift toward long wavelengths as the incident angle increases, which is in contrast to the conventional blueshift gaps. Different from

*jiang-haitao@tongji.edu.cn
†dgqql@sdu.edu.cn

using the phase variation compensation effect in Refs. [22] and [23], we let the absolute value of the phase-variation in HMM be larger than that in dielectric, which leads to the redshift property of the gap edges for TM polarization. However, it should be pointed out that the iso-frequency curve in such a HMM is still circular for transverse electric (TE) polarization. In other words, this kind of gap is still blueshifted for TE waves. Therefore, for different polarizations, the gaps will shift toward opposite directions as the incident angle increases. This property can be utilized for polarization beam selectors (PBSs) around the wavelength of the gap edge. PBSs, which can select TE- or TM-polarized light, have a tremendous number of applications in Q switched lasers [26], read-write magneto-optical data storage [27], and LCDs [28]. The well-known physical mechanism of conventional PBSs is based on the Brewster angle effect [29]. The reflectance for TM-polarized light will vanish when the incident angle reaches the Brewster angle. However, such a PBS can only work in a narrow angle range around the Brewster angle [30]. For example, the operating angle range of the PBS based on a molybdenum-yttrium multilayer is about 14° [31]. Different from conventional PBSs based on the Brewster angle effect, our PBS can work in a broader angle range.

This paper is organized as follows. In Sec. II, we show the theoretical analysis and derive the analytic conditions of the redshift gap. Then, we design the 1DPC composed of silver (Ag) and titanium dioxide (TiO_2) films. The numerical simulation of the redshift gap for TM polarization is also given. In Sec. III, we fabricate the sample and experimentally verify the redshift gap for TM polarization. The blueshift gap for TE polarization and the redshift gap for TM polarization can be utilized for efficient wide-angle polarization selection, as is demonstrated by simulation and experiment. Finally, the conclusion is given in Sec. IV.

II. THEORY ANALYSIS AND NUMERICAL SIMULATIONS

Before we study the 1DPC containing HMMs, we first see a conventional all-dielectric 1DPC denoted by $(AB)^{10}$, where A and B represent silicon dioxide (SiO_2) and TiO_2 with refractive indices of $n_A = 1.43$ and $n_B = 2.12$ [32] and thicknesses of d_A and d_B, respectively. Here, we set $n_A d_A = n_B d_B = \lambda_0/4$, where $\lambda_0 = 410.0\,\text{nm}$ is the center wavelength of the first band gap. The incident and exit media are air and BK7 (borosilicate crown glass with a refractive index of 1.52), respectively. According to the transfer matrix method [33], we calculate the reflection spectrum as a function of incident angle for both TM and TE waves, as shown in Fig. 1. The blue dashed lines represent two gap edges. With the increase in the incident angle, gap edges will shift toward short wavelengths regardless of the polarization. This blueshift phenomenon can be explained by the Bragg condition.

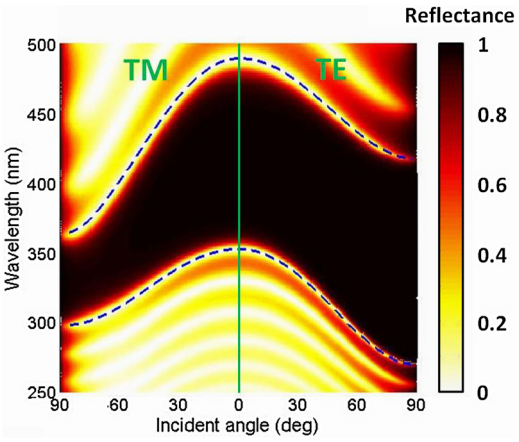

FIG. 1. Reflection spectrum of $(AB)^{10}$ vs incident angle for TM and TE polarizations. A and B represent SiO_2 and TiO_2 layers with refractive indices of $n_A = 1.43$ and $n_B = 2.12$, thicknesses of $d_A = 71.7\,\text{nm}$ and $d_B = 48.3\,\text{nm}$, respectively. Blue dashed lines represent two gap edges.

The Bragg condition of the first band gap can be given by

$$\Phi = (k_{Az} d_A + k_{Bz} d_B)|_{\lambda_{\text{Bragg}}} = \pi, \tag{1}$$

where Φ represents the propagating phase in a unit cell, k_{Az} and k_{Bz} represent the z component of the wave vectors in the A and B layers, and λ_{Bragg} denotes the Bragg wavelength. For isotropic dielectric layers A and B, we have $k_{A(B)z} = 2\pi/\lambda\sqrt{n_{A(B)}^2 - \sin^2\theta}$. Therefore, as the incident angle θ increases, the wavelength will become shorter in order to maintain the Bragg condition.

Now we change the A layer into a type-I electric HMM layer ($\varepsilon_{Ax} > 0, \varepsilon_{Az} < 0, \mu_A = 1$) [25] with an anisotropic permittivity tensor diag $(\varepsilon_{Ax}, \varepsilon_{Ax}, \varepsilon_{Az})$ and deduce the analytic conditions of the redshift gap. If $\partial\Phi/\partial\theta > 0$, the propagating phase Φ will increase with the increase in the incident angle for a fixed wavelength. As a result, the Bragg wavelength λ_{Bragg} will become longer and thus there is a redshift gap. Since $\partial\Phi/\partial\theta = (\partial\Phi/\partial k_x)(\partial k_x/\partial\theta)$ and $\partial k_x/\partial\theta = k_0\cos\theta > 0$, we only need $\partial\Phi/\partial k_x > 0$. Next, we differentiate Eq. (1) with respect to k_x and obtain

$$\frac{\partial\Phi}{\partial k_x} = \left|\left(\frac{\partial k_{Az}}{\partial k_x} d_A + \frac{\partial k_{Bz}}{\partial k_x} d_B\right)\right|_{\lambda_{\text{Bragg}}} > 0. \tag{2}$$

For the HMM layer, the iso-frequency equations for TM and TE waves can be expressed as [25]

$$\begin{aligned} &\frac{k_x^2}{\varepsilon_{Az}} + \frac{k_{Az}^2}{\varepsilon_{Ax}} = k_0^2 \ (\text{TM wave}) \ \text{and} \\ &k_x^2 + k_{Az}^2 = \varepsilon_{Ax} k_0^2 \ \ (\text{TE wave}). \end{aligned} \tag{3}$$

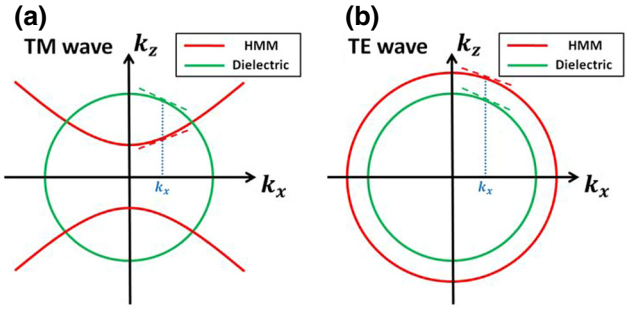

FIG. 2. Iso-frequency curves of HMM and dielectric for (a) TM and (b) TE waves. Red and green dashed lines represent the slopes of iso-frequency curves of the HMM and dielectric, respectively.

For the dielectric layer, the iso-frequency equations for TM and TE waves can be written as the same expression:

$$k_x^2 + k_{Bz}^2 = \varepsilon_B k_0^2 (\text{TM and TE waves}). \tag{4}$$

For TM polarization, the iso-frequency curves of the HMM and dielectric are a hyperbola and a circle, as shown in Fig. 2(a). The red and green dashed lines represent the slopes of the iso-frequency curves of the HMM and dielectric, respectively. We have a positive $\partial k_{Az}/\partial k_x$ and a negative $\partial k_{Bz}/\partial k_x$. Therefore, the value of $\partial\Phi/\partial k_x$ can be positive, zero, or negative, leading to a redshift, zeroshift, or blueshift gap. In a previous paper (Ref. [22]), the case of $\partial\Phi/\partial k_x = 0$ was discussed in detail. Here, we focus on the case of $\partial\Phi/\partial k_x > 0$. Following a detailed derivation (see Appendix), we can finally obtain two analytical conditions of redshift gap

$$\begin{aligned} d_A &> \frac{\lambda_{\text{Bragg}}}{2}\frac{1}{\sqrt{\varepsilon_{Ax}}[1-(\varepsilon_B/\varepsilon_{Az})]} = d_{A\,\min} \text{ and} \\ d_B &= \frac{(\lambda_{\text{Bragg}}/2) - \sqrt{\varepsilon_{Ax}}d_A}{\sqrt{\varepsilon_B}}. \end{aligned} \tag{5}$$

Then we consider the case of TE polarization. The iso-frequency curves for the HMM and dielectric are both circles [see Fig. 2(b)], and thus result in a negative $\partial k_{Az}/\partial k_x$ and a negative $\partial k_{Bz}/\partial k_x$. Hence, the sign of $\partial\Phi/\partial k_x$ must be negative, leading to a blueshift gap.

Now we design the 1DPC. The HMM layer A is mimicked by a subwavelength TiO_2/Ag multilayer, denoted by $(CD)^S$. For the isotropic dielectric layer B, we choose TiO_2 because of its high refractive index in visible wavelengths [23,32]. The whole structure is denoted by $[(CD)^S B]^N$. We choose $S=2$ and $N=3$ because a large number of Ag layers will make the fabrication difficult. The optical constants of Ag are taken from Ref. [34]. The filling ratio of TiO_2 is chosen to be 0.5. According to the effective medium theory [25], the multilayer $(CD)^S$ can be treated as a type-I HMM in the wavelength ranging from 323.6 to 412.2 nm. Here, the Bragg wavelength is set to be $\lambda_{\text{Bragg}} = 386.0$ nm. According to Eq. (5), $d_{A\,\min} = 126.2$ nm can be obtained. We choose the thickness of the HMM layer $d_A = 136.0\,\text{nm} > d_{A\,\min}$ and obtain the thickness of the dielectric layer $d_B = 30.0$ nm. For $S=2$, we finally have $d_C = d_D = 34.0$ nm. Supposing that the incident and exit media are air and BK7 (with a refractive index of 1.52), we calculate the reflection spectrum vs incident angle for TM and TE waves, as shown in Fig. 3. The blue dashed lines denote two gap edges.

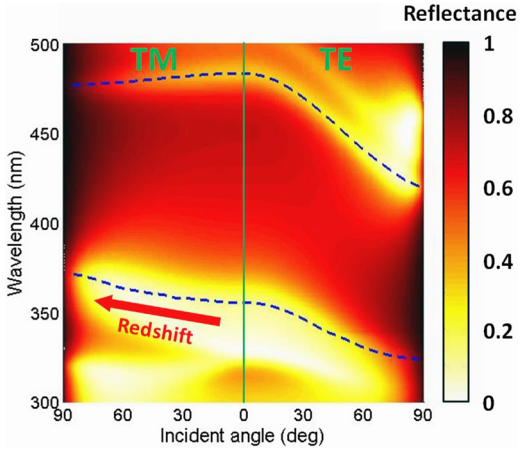

FIG. 3. Simulated reflection spectrum of $[(CD)^2B]^3$ vs incident angle for TM and TE polarizations. C and B represent TiO_2 layers with thicknesses of $d_C = 34.0$ nm and $d_B = 30.0$ nm, while D denotes a Ag layer with a thickness of $d_D = 34.0$ nm. Blue dashed lines represent two gap edges.

From the simulated results in Fig. 3, one can see that the short-wavelength gap edge is redshifted for TM polarization, while both short- and long-wavelength gap edges are blueshifted for TE polarization, which agrees with our theoretical prediction. Notice that the long-wavelength gap edge does not exhibit a redshift property for TM polarization. This is due to the fact that the long-wavelength gap edge falls outside the type-I HMM wavelength range of $(CD)^S$. Owing to the dispersion law of the permittivity of silver, the type-I HMM wavelength range of $(CD)^S$ is too narrow (from 323.6 to 412.2 nm) to simultaneously cover two gap edges.

Interestingly, the short-wavelength gap edges for two different polarizations will shift toward opposite directions as the incident angle increases. For TM polarization, the short-wavelength gap edge shifts from 355.8 to 370.5 nm when the incident angle increases from 0° to 80°. While for TE polarization, the short-wavelength gap edge shifts from 355.8 to 325.0 nm. For an incident angle larger than 30°, the wavelength $\lambda = 358.0$ nm falls outside the gap in the case of TM polarization, while it falls inside the gap in the case of TE polarization. This property can be utilized for wide-angle polarization selection, as we will discuss in the next section.

III. EXPERIMENTAL MEASUREMENTS

Based on the design in Sec. II, we fabricate the corresponding sample $[(CD)^2B]^3$ using an ion-assisted electron-beam evaporation process under high vacuum conditions. Figure 4 gives the SEM image of the sample using a Nova NanoSEM 450. The reflection spectra of the sample at different incident angles for TM and TE polarizations are measured by a Perkin Elmer LAMBDA 1050 ultraviolet-visible-near-infrared spectrophotometer with TAMS Measurement System, as shown in Figs. 5(a) and 5(b), respectively. The solid dot represents the reflectance dip of the short-wavelength gap edge. The gray shadow region indicates the variation region of the short-wavelength gap edge.

From the measured reflection spectra in Figs. 5(a) and 5(b), one can clearly see that the short-wavelength gap edge is redshifted for TM polarization, while it is blueshifted for TE polarization. In detail, the short-wavelength gap edge shifts from 355.5 to 375.0 nm when the incident angle increases from 10° to 80° for TM polarization, while for TE polarization, the short-wavelength gap edge shifts from 354.0 to 336.5 nm.

In Fig. 6, we also plot the simulated and measured short-wavelength gap edges (determined by the reflectance dip) as a function of the incident angle for TM and TE waves. The black dashed line and red crosshair represent the simulated and measured gap edges, respectively. We measure eight cases of oblique incidence in total, ranging from 10° to 80° with a step of 10°. We can conclude that the shift trend of the measured gap edge with the increase in the incident angle agrees with the simulated one. However, the wavelength of the measured gap edge slightly deviates from the simulated one, which originates from the errors in refractive index discrepancies between the experimental materials and the simulated data and the layer thickness monitoring error during the deposition process.

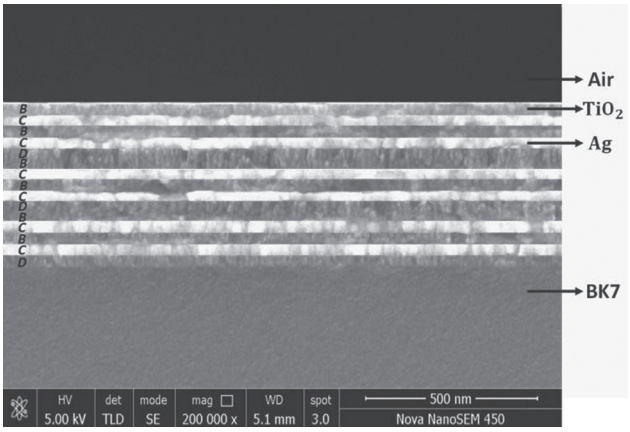

FIG. 4. SEM image of the sample $[(CD)^2B]^3$.

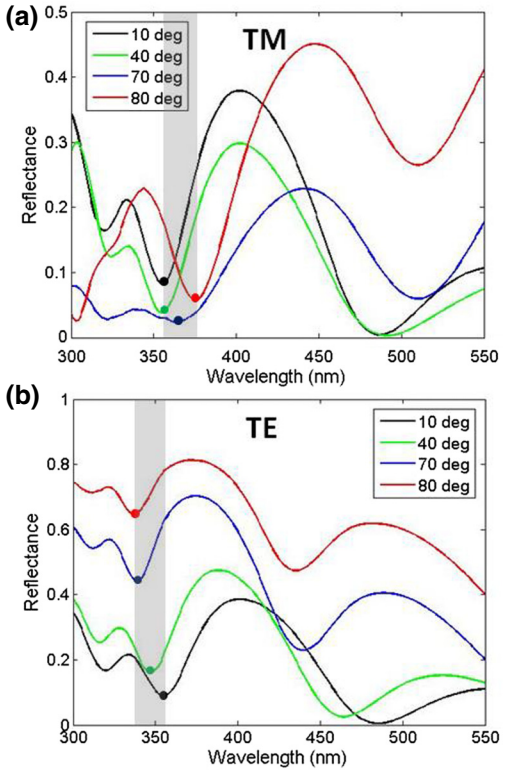

FIG. 5. Measured reflection spectra of the sample $[(CD)^2B]^3$ at four incident angles for (a) TM and (b) TE polarizations. Solid dot represents the reflectance dip of the short-wavelength gap edge. Gray shadow region indicates the variation region of the short-wavelength gap edge.

Finally, we show the polarization selection performance of the sample. Figures 7(a) and 7(b) give the simulated reflectances for TM and TE polarizations and the corresponding polarization selection ratio $\rho = R^{\mathrm{TE}}/R^{\mathrm{TM}}$ as a function of incident angle at $\lambda = 358.0$ nm. We define the angle region in which $\rho > 5$ is the efficient polarization

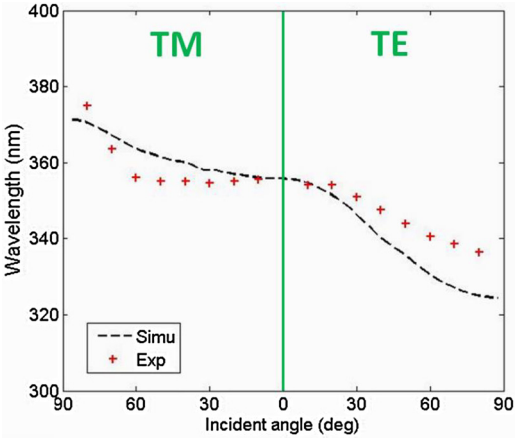

FIG. 6. Measured and simulated short-wavelength gap edges vs incident angle for TM and TE waves.

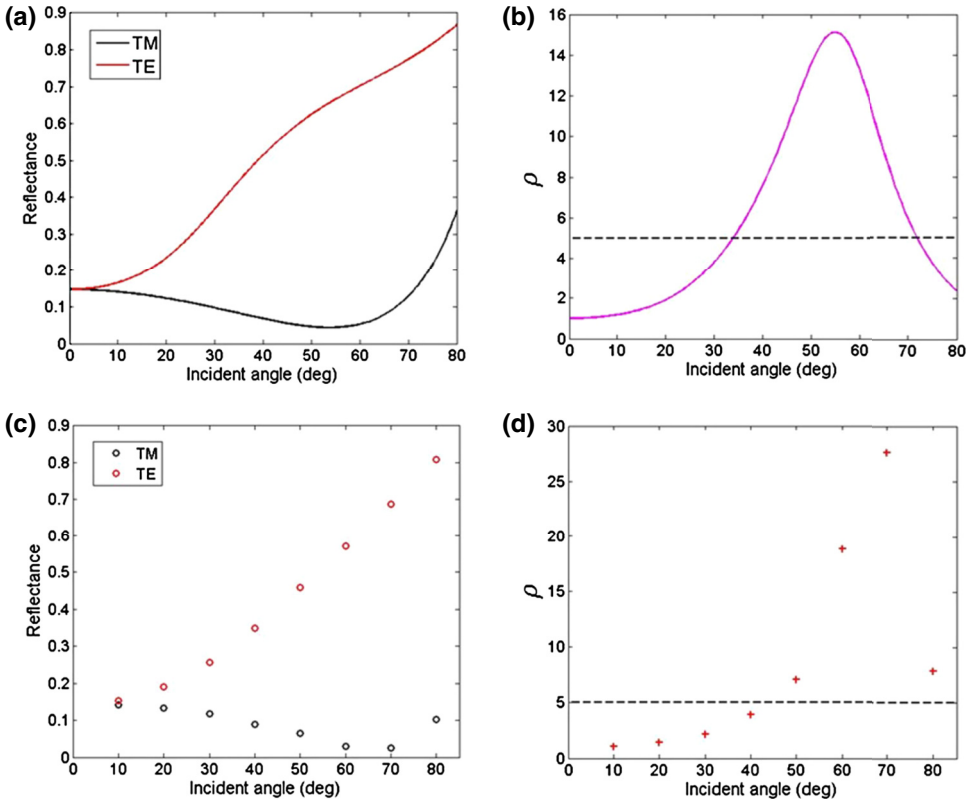

FIG. 7. (a) Simulated reflectance for TM and TE polarizations and (b) the corresponding polarization selection ratio vs incident angle at the wavelength of 358.0 nm. (c) Measured reflectance for TM and TE polarizations and (d) the corresponding polarization selection ratio vs incident angle at the wavelength of 365.0 nm. Black dashed lines represent $\rho = 5$.

selection angle region. In addition, the corresponding measured results at $\lambda = 365.0$ nm are given in Figs. 7(c) and 7(d). Here, the operating wavelength for the polarization selection in our simulation is slightly different from that in our measurement, which is induced by the difference between the simulated reflectance spectrum (Fig. 3) and the measured reflectance spectrum (Fig. 5).

From Figs. 7(a) and 7(c), we can clearly see that the reflectance always remains at low values for TM polarization, while it increases intensively for TE polarization with the increase in the incident angle, which leads to a high polarization selection ratio at broad angle ranges in Figs. 7(b) and 7(d). From our experimental measurements, the efficient polarization selection angle region ranges from 50° to 80°, indicating that our sample can be utilized for high-efficiency wide-angle polarization selection. The highest polarization selection ratio reaches 27.6 at the incident angle of 70°. It should be pointed out that the absorptances for TM and TE polarizations are high due to the loss of Ag layers, which makes the transmittances low. Therefore, it is better to utilize the sample composed of Ag and TiO_2 for the reflection-type polarization selection compared to the transmission-type one.

IV. CONCLUSIONS

In summary, we presented theoretical analysis, numerical simulation, and experimental verification of redshift gaps in 1DPCs containing layered HMMs and dielectrics for TM polarization. The redshift property of gaps originates from the anomalous wavevector dispersion of HMMs. However, the gaps are still blueshifted for TE polarization. Therefore, the edges of such gaps can be utilized for efficient wide-angle polarization selection. Our work provides another kind of physical mechanism to design high-efficiency wide-angle polarization selectors.

ACKNOWLEDGMENTS

This work is sponsored by the National Key Research Program of China (Grant No. 2016YFA0301101), by the National Natural Science Foundation of China (Grants No. 11774261, No. 11474220, No. 61621001, and No. 61661007), by the Science Foundation of Shanghai (Grant No. 17ZR1443800), by the Shanghai Science and Technology Committee (Grant No. 18JC1410900), by the Natural Science Foundation of Guangxi Province (Grant No. 2016GXNSFAA380198), by the Natural Science Foundation of Shandong Province (Grant No. ZR2015AM008), open project of State Key Laboratory of Surface Physics and Department of Physics (Grant No. KF2017_01), and by Key Laboratory of Micro and Nano-Photonic Structures (Ministry of Education).

F.W. and G.L. contributed equally to this work.

APPENDIX

Here we present a derivation on two conditions for a redshift gap. For TM polarization, we rewrite Eqs. (3)

and (4) as $k_{Az} = k_0 \varepsilon_{Ax}^{1/2}[1 - k_x^2/(\varepsilon_{Az} k_0^2)]^{1/2}$ and $k_{Bz} = k_0 \varepsilon_B^{1/2}[1 - k_x^2/(\varepsilon_B k_0^2)]^{1/2}$. Under the conditions of $|\varepsilon_{Az}| \gg 1$ and $\varepsilon_B \gg 1$, k_{Az} and k_{Bz} can be Taylor expanded to the first-order series, i.e.,

$$k_{Az} \approx k_0 \sqrt{\varepsilon_{Ax}} \left(1 - \frac{k_x^2}{2\varepsilon_{Az} k_0^2}\right) \quad \text{and}$$
$$k_{Bz} \approx k_0 \sqrt{\varepsilon_B} \left(1 - \frac{k_x^2}{2\varepsilon_B k_0^2}\right). \tag{A1}$$

Substituting Eq. (A1) into Eq. (2), we have

$$\frac{d_A}{d_B} > \frac{-\varepsilon_{Az}}{\sqrt{\varepsilon_{Ax}\varepsilon_B}}. \tag{A2}$$

At normal incidence, the Bragg condition can be given by

$$2(\sqrt{\varepsilon_{Ax}} d_A + \sqrt{\varepsilon_B} d_B) = \lambda_{\text{Bragg}}. \tag{A3}$$

Combining Eq. (A2) with Eq. (A3), we finally obtain two conditions for a redshift gap

$$d_A > \frac{\lambda_{\text{Bragg}}}{2} \frac{1}{\sqrt{\varepsilon_{Ax}}[1 - (\varepsilon_B/\varepsilon_{Az})]} = d_{A\,\text{min}} \quad \text{and}$$
$$d_B = \frac{(\lambda_{\text{Bragg}}/2) - \sqrt{\varepsilon_{Ax}} d_A}{\sqrt{\varepsilon_B}}. \tag{A4}$$

[1] E. Yablonovitch, Inhibited Spontaneous Emission in Solid-State Physics and Electronics, Phys. Rev. Lett. **58**, 2059 (1987).

[2] M. J. A. de Dood, A. Polman, and J. G. Fleming, Modified spontaneous emission from erbium-doped photonic layer-by-layer crystals, Phys. Rev. B **67**, 115106 (2003).

[3] S. John, Strong Localization of Photons in Certain Disordered Dielectric Superlattices, Phys. Rev. Lett. **58**, 2486 (1987).

[4] X. Liu, T. Shimada, R. Miura, S. Iwamoto, Y. Arakawa, and Y. K. Kato, Localized Guided-Mode and Cavity-Mode Double Resonance in Photonic Crystal Nanocavities, Phys. Rev. Appl. **3**, 014006 (2015).

[5] A. Mekis, J. C. Chen, I. Kurland, S. Fan, P. R. Villeneuve, and J. D. Joannopoulos, High Transmission Through Sharp Bends in Photonic Crystal Waveguides, Phys. Rev. Lett. **77**, 3787 (1996).

[6] Z. Li and K. Ho, Light propagation in semi-infinite photonic crystals and related waveguide structures, Phys. Rev. B **68**, 155101 (2003).

[7] S. Bhattacharya and S. John, Designing High-Efficiency Thin Silicon Solar Cells Using Parabolic-Pore Photonic Crystals, Phys. Rev. Appl. **9**, 044009 (2018).

[8] F. Qiao, C. Zhang, J. Wan, and J. Zi, Photonic quantum-well structures: Multiple channeled filtering phenomena, Appl. Phys. Lett. **77**, 3698 (2000).

[9] Y. Fink, J. N. Winn, S. Fan, C. Chen, J. Michel, J. D. Joannopoulos, and E. L. Thomas, A dielectric omnidirectional reflector, Science **282**, 1679 (1998).

[10] X. Hu, P. Jiang, C. Ding, H. Yang, and Q. Gong, Picosecond and low-power all-optical switching based on an organic photonic-bandgap microcavity, Nat. Photonics **2**, 185 (2008).

[11] J. N. Winn, Y. Fink, S. Fan, and J. D. Joannopoulos, Omnidirectional reflection from a one-dimensional photonic crystal, Opt. Lett. **23**, 1573 (1998).

[12] H. N. S. Krishnamoorthy, Z. Jacob, E. Narimanov, I. Kretzschmar, and V. M. Menon, Topological transitions in metamaterials, Science **336**, 205 (2012).

[13] T. Tumkur, G. Zhu, P. Black, Yu. A Barnakov, C. E. Bonner, and M. A. Noginov, Control of spontaneous emission in a volume of functionalized hyperbolic metamaterial, Appl. Phys. Lett. **99**, 151115 (2011).

[14] D. Lu, J. J. Kan, E. E. Fullerton, and Z. Liu, Enhancing spontaneous emission rates of molecules using nanopatterned multilayer hyperbolic metamaterials, Nat. Nanotech. **9**, 48 (2014).

[15] Z. Liu, H. Lee, Y. Xiong, C. Sun, and X. Zhang, Far-field optical hyperlens magnifying sub-diffraction-limited objects, Science **315**, 1686 (2007).

[16] Z. Jacob, L. V. Alekseyev, and E. Narimanov, Optical hyperlens: Far-field imaging beyond the diffraction limit, Opt. Express **14**, 8247 (2006).

[17] B. D. F. Casse, W. T. Lu, Y. J. Huang, E. Gultepe, L. Menon, and S. Sridhar, Super-resolution imaging using a three-dimensional metamaterials nanolens, Appl. Phys. Lett. **96**, 023114 (2010).

[18] X. Yang, J. Yao, J. Rho, X. Yin, and X. Zhang, Experimental realization of three-dimensional indefinite cavities at the nanoscale with anomalous scaling laws, Nat. Photonics **6**, 450 (2012).

[19] C. Wu, A. Salandrino, X. Ni, and X. Zhang, Electrodynamical Light Trapping Using Whispering-Gallery Resonances in Hyperbolic Cavities, Phys. Rev. X **4**, 021015 (2014).

[20] Z. Huang and E. E. Narimanov, Zeroth-order transmission resonance in hyperbolic metamaterials, Opt. Express **21**, 15020 (2013).

[21] Z. Saleki, S. R. Entezar, and A. Madani, Optical properties of a one-dimensional photonic crystal containing a graphene-based hyperbolic metamaterial defect layer, Appl. Opt. **56**, 317 (2017).

[22] C. Xue, Y. Ding, H. Jiang, Y. Li, Z. Wang, Y. Zhang, and H. Chen, Dispersionless gaps and cavity modes in photonic crystals containing hyperbolic metamaterials, Phys. Rev. B **93**, 125310 (2016).

[23] F. Wu, G. Lu, C. Xue, H. Jiang, Z. Guo, M. Zheng, C. Chen, G. Du, and H. Chen, Experimental demonstration of angle-independent gaps in one-dimensional photonic crystals containing layered hyperbolic metamaterials and dielectrics at visible wavelengths, Appl. Phys. Lett. **112**, 041902 (2018).

[24] A. Poddubny, I. Iorsh, P. Belov, and Y. Kivshar, Hyperbolic metamaterials, Nat. Photonics **7**, 948 (2013).

[25] L. Ferrari, C. Wu, D. Lepage, X. Zhang, and Z. Liu, Hyperbolic metamaterials and their applications, Prog. Quantum Electron. **40**, 1 (2015).

[26] J. Yang, L. Wang, X. Wu, T. Cheng, and H. Jiang, High peak power Q-switched Er:YAG laser with two polarizers and its ablation performance for hard dental tissues, Opt. Express **22**, 15686 (2014).

[27] R. K. Kostuk, T. J. Kim, G. Campbell, and C. W. Han, Diffractive-optic polarization-sensing element for magneto-optic storage heads, Opt. Lett. **19**, 1257 (1994).

[28] M. Xu, H. P. Urbach, D. K. G. de Boer, and H. J. Cornelissen, Wire-grid diffraction gratings used as polarizing beam splitter for visible light and applied in liquid crystal on silicon, Opt. Express **13**, 2303 (2005).

[29] L. Li and J. A. Dobrowolski, High-performance thin-film polarizing beam splitter operating at angles greater than the critical angle, Appl. Opt. **39**, 2754 (2000).

[30] D. Blanc, P. H. Lissberger, and A. Roy, The design, preparation and optical measurement of thin film polarizers, Thin Solid Films **57**, 191 (1979).

[31] Z. Wang, H. Wang, J. Zhu, Y. Xu, S. Zhang, C. Li, F. Wang, Z. Zhang, Y. Wu, X. Cheng, L. Chen, A. G. Michette, S. J. Pfauntsch, A. K. Powell, F. Schäfers, A. Gaupp, and M. MacDonald, Extreme ultraviolet broadband Mo/Y multilayer analyzers, Appl. Phys. Lett. **89**, 241120 (2006).

[32] B. Liu, G. Lu, L. Cui, J. Li, F. Sun, F. Liu, Y. Li, T. Yang, and G. Du, Experimental investigation of multiple near-perfect absorptions in sandwich structures containing thin metallic films, Opt. Express **25**, 013271 (2017).

[33] P. Yeh, *Optical Waves in Layered Media* (Wiley, New York, 1988).

[34] E. Palik, *Handbook of Optical Constants of Solids* (Academic, New York, 1998).